



**Thermal effects on the electronic properties of sodium electride under high pressures**R. Paul <sup>1</sup>, S. X. Hu <sup>1,\*</sup>, V. V. Karasiev,<sup>1</sup> S. A. Bonev,<sup>2</sup> and D. N. Polsin<sup>1</sup><sup>1</sup>Laboratory for Laser Energetics, University of Rochester, 250 East River Road, Rochester, New York 14623-1299, USA<sup>2</sup>Lawrence Livermore National Laboratory, 7000 East Avenue, Livermore, California 94550, USA

(Received 18 June 2020; accepted 18 August 2020; published 11 September 2020)

Sodium is a simple metal at ambient conditions, while it transits to an electride phase at pressures above  $\sim 160$  GPa along the room-temperature isotherm. We explore the thermal effects on the electronic properties of the *hP4* phase of sodium along the  $\rho = 5.872$  g/cm<sup>3</sup> isochore. We quantitatively classify this phase as an insulator based on the criterion of nearsightedness of the one-particle density matrix. *Ab initio* calculations suggest that the band gap of this insulator decreases with increasing temperature along the isochore, primarily because of ionic distortions, culminating in an insulator-to-metal transition upon melting at  $T_m \approx 2100$  K. This transition is accompanied by residual electronic localization (in *d* orbitals) in the form of dynamic electron bubbles and a change in hybridization from *p-d* to *s-p* upon melting. This transition is explored by tracking the electronic and electro-optical properties along the isochore under consideration.

DOI: [10.1103/PhysRevB.102.094103](https://doi.org/10.1103/PhysRevB.102.094103)**I. INTRODUCTION**

Despite being one of the simplest alkali metals at ambient pressure and temperature conditions, sodium exhibits a remarkably complex behavior under compression. The first prediction pertaining to such behavior, in Neaton and Ashcroft's seminal work [1], demonstrated the possibility of electron localization in interstitial crystal lattice sites at pressures exceeding 800 GPa, where sodium was predicted to attain a structure with the *Cmce* space-group symmetry. Consequently, diamond-anvil cell (DAC) experiments performed along the room-temperature isotherm [2] have demonstrated the existence of a six-coordinated phase, *hP4*, in which increased core electron overlap decreases the symmetry of the valence electron charge distributions. The transition to *hP4* commences at approximately 160 GPa from the *tI19* phase. This phase is structurally similar to a double hexagonal close-packed (dhcp) structure and has a higher compression along the *c* axis ( $c/a = 1.391$ ) compared to the ideal dhcp ( $c/a = 3.266$ ) at 320 GPa [2]. Due to the existence of a band gap, this phase has been described as a transparent "insulator," deviating from the reflective metallic behavior observed at lower pressures. Additional experiments and calculations exploring the Raman spectra in great detail [3] have pinned down the melt and solid-solid transitions beyond 180 GPa and delved into the evolution of electron localization function (ELF) attractors with pressure. Prior to both of these experiments, a combined theoretical-experimental study used synchrotron infrared (IR) spectroscopy to investigate the evolution of optical properties of electronic origin [4]. Its conclusion was that a pseudogap opens up in the electronic density of states of the orthorhombic *oP8* phase above 118 GPa, accompanied by a decrease in IR reflectivity. One insightful calculation [5] explored the optical excitonic

properties of the *hP4* phase using the Bethe-Salpeter equation. They reported anisotropy to be a major feature of this particular phase, whereby the absorption coefficient greatly differs depending on whether the direction of incidence is perpendicular to the *c* (transparent up to  $h\nu = 3$  eV) or *ab* (transparent up to  $h\nu = 4.5$  eV) plane. However, all of these calculations were performed for static, nonthermalized crystals whereas DAC experiments have been along the  $T = 300$  K isotherm. To the best of our knowledge, there is a lack of systematic studies for the effects of thermal excitations on the electronic and electro-optical properties of solid electride sodium.

In this paper, we have used a variety of *ab initio* methods to explore the finite-temperature electronic properties of *hP4*-sodium by looking at the density of states-derived band gap, electron localization function, and electro-optical properties calculated using the Kubo-Greenwood formula. To this end, we have also extended the phase diagram of sodium up to  $\sim 500$  GPa. However, the possible existence of high-temperature solid phases other than *hP4* beyond 320 GPa has not been addressed in this paper.

The remainder of the paper is organized in three sections. Section II discusses the first-principles simulation details, the Kubo-Greenwood formulation, the quasiharmonic free-energy calculation method, and the thermal band-gap evaluation used later in this paper. Section III presents the results from such simulations and discusses these results with an emphasis on quantitative and analytic arguments. Finally, Sec. IV summarizes the paper and discusses the future scope of research on this topic.

**II. METHOD AND FORMULATION****A. Density functional theory-based calculations**

Ground-state Kohn-Sham density functional theory (DFT) [6,7] calculations were performed using the plane-wave

\*shu@lle.rochester.edu

implementation of DFT in the Vienna *Ab initio* Simulation Package (VASP) [8–10], with exchange-correlation (XC) functionals based on the generalized gradient approximation (GGA) [11] and meta-GGA [12]. For the sake of comparison of melt curve data and optics calculations, we mostly resorted to using the SCAN-L [12] XC functional, which is a deorbitalized version of the meta-GGA strongly constrained and appropriately normed (SCAN) [13] functional. However, Perdew-Burke-Ernzerhof (PBE) [14], and PBEsol [15], which is a version of PBE customized for the solid state, were also used for the comparison of the melt point and band-gap data. For determining solid-solid phase boundaries, phonon density-of-state (DOS) calculations were carried out in order to obtain phonon free energies. These were performed using PHONOPY [16,17] and VASP at the level of density-functional perturbation theory [18]. Finite-temperature electronic contributions to the free energy were also included using Mermin’s extension of Kohn-Sham DFT [19], with static ionic configurations and introducing electronic temperature via Fermi-Dirac smearing. For calculating optical properties, six snapshots from a quantum molecular-dynamics (QMD) trajectory were used to calculate the frequency-dependent dielectric response in the independent-particle approximation, with the Kubo-Greenwood formalism [20,21] for interband transitions, which we concisely discuss later. QMD simulations were performed with VASP using supercells with periodic boundary conditions as follows:  $6 \times 6 \times 6$  primitive unit cells for bcc and fcc,  $2 \times 2 \times 4$  primitive unit cells for *tI19*, and  $4 \times 4 \times 4$  primitive unit cells for *hP4*. However, due to the incommensurate host-guest nature of the *tI19* unit cell, an approximate *tI20* unit cell was used instead, which is an *I4/mcm* host lattice with sodium guest atoms at the *2b* Wyckoff sites. Such a unit cell has been shown previously [4] to be nearly equivalent electronically to *tI19*. The resulting supercells have 216 atoms for bcc and fcc, 320 for *tI19*, and 256 for *hP4*. In the QMD simulations, the reciprocal space was sampled using both the  $\Gamma$  point and the Baldereschi mean-value  $2\pi/a \times (\frac{1}{4}, \frac{1}{4}, \frac{1}{4})$  [22]  $\mathbf{k}$  point ( $a$  being the lattice constant). For the density of states and electro-optical calculations, denser  $5 \times 5 \times 5$  and  $2 \times 2 \times 2$  Monkhorst-Pack [23]  $\mathbf{k}$  meshes were used, respectively. In the QMD simulations, the  $\mathbf{k}$  resolution, being restricted by the imposition of periodic boundary conditions, ranged from  $0.397 \text{ \AA}^{-1}$  (for bcc at  $2.097 \text{ g/cm}^3$ ) to  $0.564 \text{ \AA}^{-1}$  (for *hP4* at  $5.872 \text{ g/cm}^3$ ). For static calculations, the smallest such vector accessible was always  $\leq 0.15 \text{ \AA}^{-1}$ . Ionic time-step size was 0.5 or 1.0 fs over approximately 6000 or 4000 steps, yielding a total atomistic simulation time of 3 to 4 ps. Projector augmented wave pseudopotentials [24,25] with a  $1.20 \text{ \AA}$  cutoff of core radius were used with the semicore  $2s^2 2p^6 3s^1$  electrons being treated as valence electrons, corresponding to a kinetic energy cutoff of 1000 eV for the plane-wave basis set. Electrons were populated according to Fermi-Dirac statistics and all electronic self-consistent field calculations were converged to a precision of  $10^{-5}$  eV/atom for the free energies. The details of method used in the electro-optical calculations and solid-solid phase-boundary determination have been elaborated upon in the Supplemental Material [26].

## B. Thermal evolution of electronic band gap

Using the Allen-Cardona approach [27,28], a shift in electronic energy for a band  $n$  and wave vector  $\mathbf{k}$ , due to finite displacements of  $N_a$  atoms from equilibrium, can be expressed using a Taylor series expansion as

$$\Delta E_{n,\mathbf{k}} = \mathbf{x} \cdot \frac{\partial E_{n,\mathbf{k}}}{\partial \mathbf{x}} + \frac{1}{2} \mathbf{x} \cdot \mathbf{H} \cdot \mathbf{x} + \dots, \quad (1)$$

where  $\mathbf{x}$  is a vector of  $3N_a$  displacements and  $\mathbf{H}$  is a Hessian matrix with  $3N_a \times 3N_a$  elements. For displacements along the normal mode,  $\mathbf{x}$  can be written as

$$x_\alpha = \sum_j \left( \frac{\hbar}{2m\omega_j} \right)^{1/2} P_{\alpha,j} (a_j + a_j^\dagger), \quad (2)$$

where  $\alpha$  denotes direction,  $a_j$  and  $a_j^\dagger$  denote the creation and annihilation operators, respectively, and  $P_{\alpha,j}$  is the polarization vector. Substituting Eq. (2) into Eq. (1) in the harmonic approximation, after truncating at the second-order term, results in the linear term vanishing and the resulting expression being

$$\Delta E_{n,\mathbf{k}} = \sum_j \frac{\partial E_{n,\mathbf{k}}}{\partial n_{B,j}} \left( \frac{1}{2} + n_{B,j} \right) \equiv \Delta E_{g,\text{harmonic}} \quad (3)$$

with  $n_{B,j}$  being the Bose-Einstein distribution factor for phonon mode  $j$  containing the implicit thermal dependence, and  $\partial E_{n,\mathbf{k}}/\partial n_{B,j}$  being the phonon-electron coupling coefficient.

## III. RESULTS AND DISCUSSION

For all intents and purposes, studying the solid phase at near-melt temperatures necessitates establishing an upper bound for the solid state, i.e., a melt curve. The melt curve was formally established by performing QMD simulations in VASP using a canonical (constant-*NVT*) ensemble. Such *NVT* simulations were performed along an isochoric path while gradually increasing the ensemble temperature. This is termed as the *heat until melt* method and the temperature regulation was attained using a Nosé-Hoover thermostat [29]. The melt curve for the *tI19*- and *hP4*-to-liquid transition demonstrates a monotonically increasing behavior as pressure increases, as can be seen in Fig. 1. This is true even for the isochore starting at  $P = 1000 \text{ GPa}$  along the cold curve (not shown in Fig. 1), for which we evaluated the melt point to be in between 6000 and 7000 K, implying the melt curve has a positive slope up to at least  $\sim 1 \text{ TPa}$ . We used *NVT* simulations and tracked the changes in pressure and the radial distribution function, with temperature, to determine the melt point ( $T_m$ ) along each isochore. This method has also been used to determine the melt curve of silicon under high pressures [31,32], which gave reasonable agreement with experiments. In general, PBE and PBEsol were observed to agree within 100 K once a proper fit is introduced. However, the melt curve calculated using SCAN-L substantially differs from the former two. We used the Kechin fit [33],

$$T_{\text{melt}}(P) = T_0 \left( 1 + \frac{P_{\text{melt}} - P_0}{a} \right)^b e^{-c(P_{\text{melt}} - P_0)} \quad (4)$$

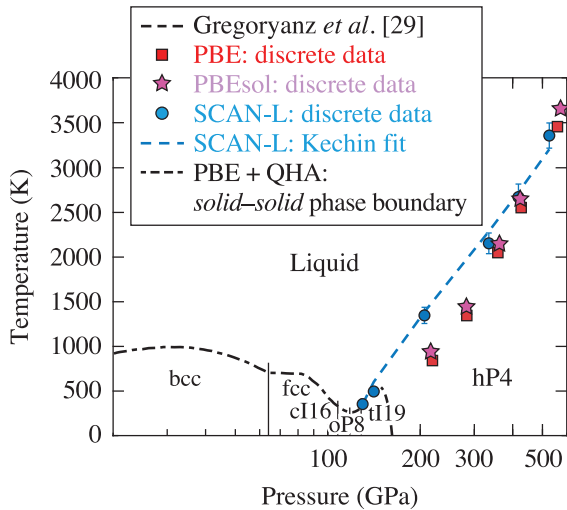


FIG. 1. The  $T$ - $P$  phase diagram of sodium from literature [30] combined with our work, with the existing melt curve data plotted. The  $tI19$  –  $hP4$  phase boundary was constructed by comparing the Gibbs free energy computed by combining DFT and quasiharmonic approximated (QHA) calculations. The  $T$ - $P$  melt points from DFT calculations using SCAN-L exchange-correlation functional have been fitted with a Kechin equation as described in the text. The uncertainty for the six isochoric melt data points, calculated using SCAN-L, are 20, 35, 90, 115, 145, and 140 K, respectively, calculated using five separate sets of MD calculations, with differing starting solid geometry, for each isochore.

on the SCAN-L data, with  $a = 7.1535$ ,  $b = 0.5465$ , and  $c = -0.00008464$ , and show it in Fig. 1 since our electro-optical calculations also use the SCAN-L exchange-correlation functional. In addition to the *heat until melt* method mentioned above, *two-phase coexistence* simulations were also performed along the  $\rho = 5.011$  and  $5.872$  g/cm<sup>3</sup> isochores using 512 atoms in a supercell. Of these 512 atoms, 256 were arranged in  $hP4$  symmetry (solid) and the remaining 256 were randomly arranged (liquid).  $NVT$  simulations, using the SCAN-L exchange-correlation functional, with a Nosé-Hoover thermostat were performed using a temperature step size of 100 K. The resulting  $T_m$  obtained were 1350 and 2050 K for the  $\rho = 5.011$ - and  $5.872$ -g/cm<sup>3</sup> isochores, respectively (see sec. III of the Supplemental Material [26]). This would imply that at least within the range of the isochores starting in between 260 and 320 GPa along the  $T = 0$  K isotherm, the  $T_m$  measured using the *heat until melt* method is higher than that obtained from the *two-phase coexistence* simulations by 100 to 200 K.

The  $tI19$ - $hP4$  phase boundary obtained from Gibbs free-energy comparison, including the electronic-thermal Helmholtz free energy, ionic zero-point Helmholtz free energy, the quasiharmonic ionic-thermal Helmholtz free energy sans any anharmonic corrections, and the thermal pressure-volume work, exhibit a negative slope in  $T$ - $P$  space (see Fig. 1). For the purpose of all isochoric analyses to follow, we used a particular isochore corresponding to  $\rho = 5.872$  g/cm<sup>3</sup>, which starts at  $P = 320$  GPa along the  $T = 0$  K isotherm. Since the starting pressure is far away from the  $tI19$ - $hP4$

transition pressure along the cold curve, even if anharmonicity completely changes the transition boundary between the  $tI19$  and  $hP4$  phases, the isochore under consideration would still be expected to be in the  $hP4$  phase. In terms of the higher-pressure transition along the cold curve, it has already been predicted that the  $hP4$  phase reverts back to the orthorhombic  $oP8$  phase at  $\sim 1.75$  TPa [34]. One feature worth pointing out is that the  $cla$  axial ratio of  $hP4$  decreases with increasing pressures from 1.5482 ( $P = 180$  GPa) to 1.3908 ( $P = 320$  GPa) to 1.3385 ( $P = 500$  GPa), according to our calculations. This implies higher compressibility along the  $c$  axis, indicating the higher compaction along the  $CACB$ ... stacking planes even at lower pressures. This is the geometric feature responsible for the anisotropy in the absorption spectra of  $hP4$  [5]. Correspondingly, the volume per atom (in Å<sup>3</sup>/atom) varies from 8.27 ( $P = 180$  GPa) to 6.52 ( $P = 320$  GPa) to 5.43 ( $P = 500$  GPa).

The existence of a high-temperature solid phase different from  $hP4$  was also explored using  $NPT$ -QMD calculations. First, we used 128-, 162-, 192-, 216-, 256-, and 320-atom supercells and induced melting in each by incrementally increasing the temperature by steps of 100 K along the  $P = 320$  GPa isobar while allowing cell relaxation. This ensures that all unit cells with 1 to 6 atoms or multiples are covered. Upon obtaining the molten liquid-phase supercell at  $T = 2300$  K, we froze the supercell using  $NPT$ -QMD by 100 K steps using a cooling rate of  $5 \times 10^{12}$  K/s. The resulting most-stable (energetically) supercell was still the  $hP4$ -derived one. However, this does not rule out the existence of different high-temperature phases at higher pressures. Preliminary calculations along the  $P = 400$  GPa isobar suggests the existence of a distorted hexagonal structure at high temperatures which is a subject of future work, while the current focus is on the thermal effects on the electronic and optical properties of  $hP4$  only.

Formally, the orthonormalized single-particle Kohn-Sham orbitals  $|\Psi_n^{KS}\rangle$  can be used to construct the one-particle density operator  $\hat{\rho}_1 = \sum_n f_{FD,n} |\Psi_n^{KS}\rangle \langle \Psi_n^{KS}|$ , where  $f_{FD,n}$  is the Fermi-Dirac weight of the  $n$ th orbital, which in turn can be used to create the one-particle density matrix

$$\begin{aligned} \rho_1(\mathbf{r}, \mathbf{r}') &= \langle \mathbf{r} | \hat{\rho}_1 | \mathbf{r}' \rangle = \sum_n f_{FD,n} |\Psi_{KS,n}(\mathbf{r})\rangle \langle \Psi_{KS,n}(\mathbf{r}')| \\ &\equiv N \int d\mathbf{r}_2 \dots d\mathbf{r}_N \Psi_{KS,n}^*(\mathbf{r}', \mathbf{r}_2, \dots, \mathbf{r}_N) \\ &\quad \times \Psi_{KS,n}(\mathbf{r}, \mathbf{r}_2, \dots, \mathbf{r}_N), \end{aligned} \quad (5)$$

such that  $\text{tr} \rho_1(\mathbf{r}, \mathbf{r}') = \int \rho_1(\mathbf{r}, \mathbf{r}') d\mathbf{r} = N$ . This one-particle density matrix can be constructed from the three-dimensional  $E$  versus  $\mathbf{k}$  data of the system. Integration of the band-structure points  $g(E_j, k_i)$  with respect to  $\mathbf{k}$  along a special path (i.e.,  $\oint_i g(E, k_i) d\mathbf{k}$ ) leads to the electronic density of states, whereas integration with respect to  $E$  [i.e.,  $\int_j g(E_j, \mathbf{k}) dE$ ] yields normalized on-site occupancies in the form of a diagonalized matrix  $\rho_1(\mathbf{k}, \mathbf{k}')$  as a function of  $\mathbf{k}$  eigenstates, since the off-diagonal (coherence) terms are zero after completion of electronic optimization. For our case, a  $2 \times 2 \times 2$   $\mathbf{k}$  mesh results in an  $8 \times 8$  diagonalized

reciprocal-space, one-particle density matrix. The corresponding real-space, one-particle symmetric density matrix  $\rho_1(\mathbf{r}, \mathbf{r}')$  can be obtained by Fourier back-transformation of  $\rho_1(\mathbf{k}, \mathbf{k}')$  as  $\rho_1(\mathbf{r}, \mathbf{r}') = (1/\Omega) \sum_{\mathbf{k}, \mathbf{k}'} e^{i\mathbf{k}\cdot\mathbf{r}} \langle \mathbf{k} | \hat{\rho}_1 | \mathbf{k}' \rangle e^{i\mathbf{k}'\cdot\mathbf{r}'}$ . Using *nearsightedness* as a metric for quantitatively differentiating insulators from semiconductors, we use the formulation  $\rho_1(\mathbf{r}, \mathbf{r}') \sim \langle \exp(-\gamma|\mathbf{r} - \mathbf{r}'|) \rangle$ , with  $\gamma \propto E_g^{1/2}$  for normal insulators and  $\gamma \propto E_g$  for semiconductors, where  $E_g$  is the band gap [35,36]. Along the  $\rho = 5.872 \text{ g/cm}^3$  isochore, our analyses indicate that  $\gamma$  varies with a (decreasing) band-gap exponent  $\eta$  (in  $E_g^\eta$ ) of 0.460, 0.438, 0.421, and 0.414 at  $T = 300, 700, 1200,$  and  $1800 \text{ K}$ , respectively. While we expected the value of  $\eta \approx 0.5$ , the obtained values of  $\eta < 0.5$  may be a result from using a noncubic supercell in our simulations. Despite this approximation, it is safe to state that the *hP4* phase of sodium behaves like an insulator and not a semiconductor.

The band gap obtained from the electronic DOS calculations shows a gradual decrease with increasing temperatures along the  $\rho = 5.872 \text{ g/cm}^3$  isochore until it abruptly decreases to zero upon melting, as shown by Fig. 2. Technically speaking, the abrupt drop still is not a step-function-like fall, mainly because of finite-size effects. This can be seen in Fig. 2(a), which also shows a comparison of the values calculated using PBE, PBEsol, SCAN, and SCAN-L exchange-correlation functionals. The band-gap values were obtained by averaging the electronic DOS of six atomic configuration snapshots taken from the molecular-dynamics trajectory and separated by at least 100 fs from each other. The total simulation time for this analysis was 1.6 to 2.0 ps, after 1.4 to 2.0 ps of thermal equilibration. Surprisingly, the PBE and SCAN results are closer to the experimental band gap because the experimental values are most likely higher than the calculated value using DFT, where it is worth mentioning that GW calculations are more accurate than single-particle mean-field DFT calculations [2]. At  $T = 300 \text{ K}$ , the calculated band gap was in the range of 1.54 eV (SCAN-L) to 1.84 eV (PBE), which corresponds to a photon wavelength of 673.83 nm (PBE) to 805.09 nm (SCAN-L). For wavelengths shorter than this threshold, *hP4* sodium would exhibit reflectivity resembling that of an optical insulator. Selected electronic density of states at 300, 1800, and 2500 K, shown in Fig. 2(b), clearly demonstrate the closing of the band gap and depression of the DOS peaks on either side of the Fermi level once the band gap closes. For this particular isochore under consideration, since the melt point is between 2100 and 2200 K irrespective of the exchange-correlation functional used, it is clear that there is an abrupt insulator-to-metal transition upon melting.

A detailed analysis of the band gap  $E_g$  involves breaking it up into components arising from the ionic thermal displacements ( $\Delta E_{g,i-th}$ ), the thermal modifications to the Fermi-Dirac distribution function ( $\Delta E_{g,e-th}$ ), and the phonon-electron coupling ( $\Delta E_{g,ph-e}$ ). The first and second terms are included in the band gap as calculated from DFT-QMD calculations. The third term, however, requires knowledge of  $\Delta E_{g,harmonic}$  from Eq. (3) and has to be explicitly calculated. Note that contributions originating from lattice thermal distortions can be neglected because the off-diagonal stress components ( $\sigma_{xy}$ ,  $\sigma_{yz}$ , and  $\sigma_{xz}$ ) are approximately within  $\pm 1.5\%$  of the normal stress ( $\sigma_{xx}$ ,  $\sigma_{yy}$ , and  $\sigma_{zz}$ ) values, as can be seen in Table I. The aforementioned contributions to  $E_g$  can

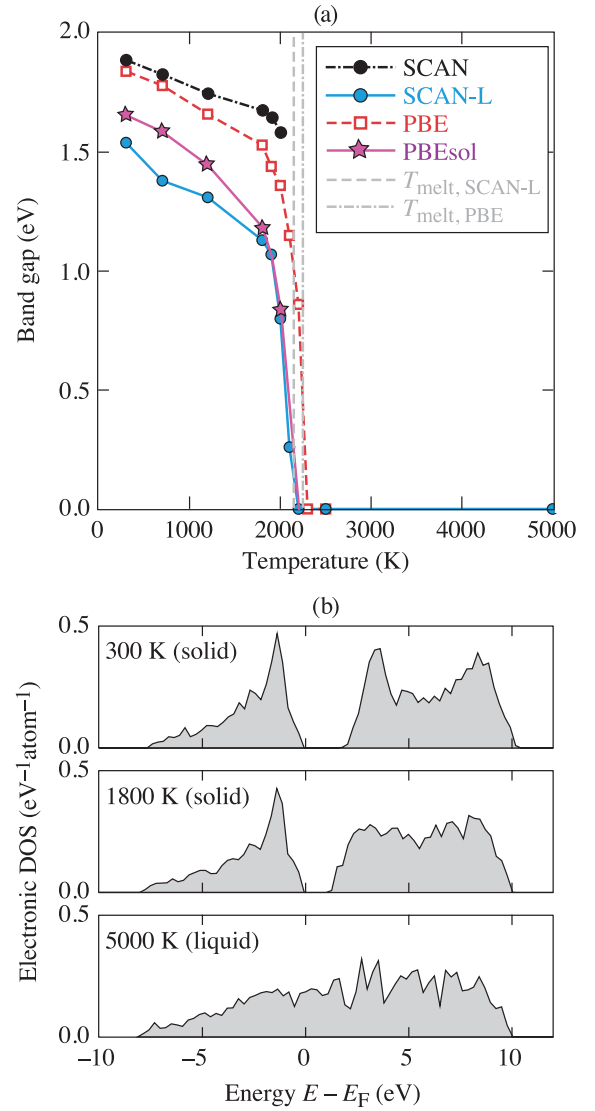


FIG. 2. (a) The evolution of the band gap with temperature during heating along the  $\rho = 5.872 \text{ g/m}^3$  isochore demonstrates the abrupt closing of the band gap on melting at  $T_m \approx 2100$  to  $2200 \text{ K}$ , corresponding to an insulator-to-metal transition. Four sets of data corresponding to different exchange-correlation functionals: PBE, PBEsol, SCAN, and SCAN-L. (b) Sample normalized electronic DOS along the  $\rho = 5.872 \text{ g/m}^3$  isochore, where the absence of the band gap can be seen in the liquid phase DOS at  $T = 5000 \text{ K}$ . Here  $E_F$  denotes the Fermi energy.

be evaluated using the following:

$$\begin{aligned} \Delta E_{g,e-th}(V, T) &= E_{g,\text{DFT}}(\Gamma; V, T_e = T) - E_{g,\text{DFT}}(\Gamma; V, T_e = 0), \end{aligned} \quad (6)$$

$$\begin{aligned} \Delta E_{g,i-th}(V, T) &= E_{g,\text{DFT}}(\Gamma; V, T_e = 0) - E_{g,\text{DFT}}(\Gamma_0; V, T_e = 0), \end{aligned} \quad (7)$$

$$\begin{aligned} \Delta E_{g,ph-e}(V, T) &= [\Delta E_{g,harmonic}(\Gamma_0; V, T_e = 0, T_i = T) \\ &\quad + E_{g,\text{DFT}}(\Gamma_0; V, T_e = 0)] \\ &\quad - E_{g,\text{DFT}}(\Gamma; V, T_e = T), \end{aligned} \quad (8)$$

TABLE I. Lattice stress anisotropy in *NVT*-QMD simulations along the  $\rho = 5.872 \text{ g/cm}^3$  isochore. All  $\sigma$  are in units of GPa.

Temperature (K)	$\sigma_{xx}$	$\sigma_{yy}$	$\sigma_{zz}$	$\sigma_{xy}$	$\sigma_{yz}$	$\sigma_{xz}$
300	330.746	331.941	329.327	0.4169	-0.1847	-0.0762
700	333.639	335.764	333.436	0.9134	-0.4712	-0.1945
1200	337.214	340.407	338.783	1.4981	-0.8275	-0.3106
1800	345.497	350.320	347.667	1.9165	-1.2334	-2.2185
2500	372.835	371.765	330.872	0.4414	-0.0324	-1.9032

where  $\Gamma$  is a frozen-ionic configuration obtained from an *NVT*-QMD trajectory with electronic temperature  $T_e = T$  and ionic temperature  $T_i = T$ ,  $\Gamma_0$  is the zero Kelvin static configuration, and  $E_g(\Gamma_0 : V, T_e = 0)$  is the band gap at  $T = 0$  K. The phonon-electron coupling constant was calculated using EPW [37]. The results are shown in Fig. 3, where it can be seen that  $\Delta E_{g,i-th}$  is the principal driver in the reduction in band gap with increasing temperatures along the isochore, and not the altered electronic distribution itself. The contribution of  $\Delta E_{g,ph-e}$  initially increases with temperature and then decreases towards zero upon approaching melting. This implies that the electronic band-gap reduction is a purely ion dynamics-mediated process.

Taking a closer look into the electronic charge distributions, it can be seen that one exceptional feature of high-pressure electriles is the localization of electrons in the interstices between ions, which leads to the formation of pockets with an ELF [38] value of near unity, existing as the pseudoanions mentioned earlier in Sec. I. Similar behavior has also been observed in the case of liquid lithium [39]. The *hP4* phase of sodium exhibits such features resulting in an insulating behavior owing to the band gap that develops

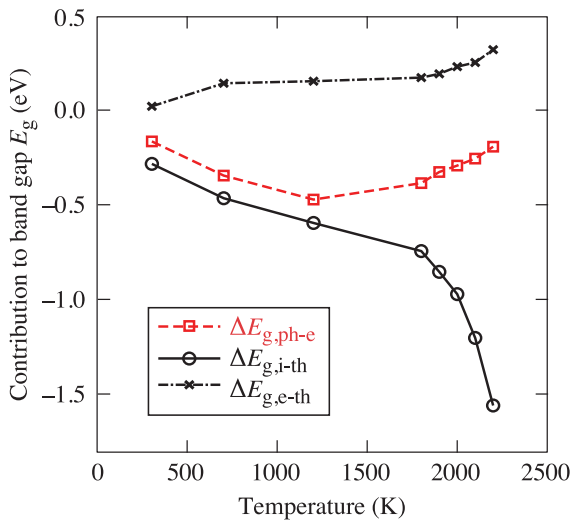


FIG. 3. The contributions of the different components of the electronic band gap illustrating the role played by ionic thermal displacements,  $\Delta E_{g,i-th}$ , in gap reduction relative to the zero Kelvin static gap,  $E_{g,static}$ . The component with a positive contribution is electronic thermal in nature due to temperature-dependent alterations to the Fermi-Dirac distribution function,  $\Delta E_{g,e-th}$ . The component due to phonon-electron coupling,  $\Delta E_{g,ph-e}$ , has a negative contribution but decreases to zero near the melt curve.

from such an electronic distribution. This is true all the way up to the melt point, beyond which the system is expected to transform into a near free electron (NFE)-type liquid, with ELF values predominantly close to 0.5. While bulk electronic properties, such as the band-gap calculations shown in Fig. 2, indicate this to be the case, there is more nuance that can be understood by examining spatially localized properties, e.g., as revealed by the ELFs, as is evidenced by the planar ELF from Fig. 4. The (001) planar ELF along the  $\rho = 5.872 \text{ g/cm}^3$  isochore clearly exhibits localized clusters of paired electrons, in the form of electron bubbles of ELF values between 0.8 and 1.0, that persist even beyond the melt point, as can be seen in Fig. 4(a). Rough estimation of the total number of electrons in certain pseudoanionic attractor regions yields a value of 1.91 to 2.0 in the solid phase and 1.77 to 1.94 in the liquid phase. This implies that the ELF attractors in the liquid phase are paired as well. A different route of observation, along the  $T = 2500$  K isotherm [Fig. 4(b)] shows that this behavior gradually develops with increasing pressure.

To further examine the electron localization, we calculated all-volume charge-weighted ELF histograms, which are shown in Fig. 5. The left-hand side plots are histograms of the ELF values calculated at the three-dimensional fast Fourier transformation grids of the DFT calculations, normalized with the size of the grid. The plots in the center show the integrated ELF histograms (cumulative number of valence electrons per atom with ELF below a given value), and the right-hand side plots are the charge-weighted version of the left-hand side plots. The first peak in the left- and right-hand side plots (ELF  $\approx 0.1$ ) correspond to the space surrounding the core electrons owing to Coulombic repulsion, whereas the second peak ( $0.7 < \text{ELF} < 0.8$ ) originates from the core electrons themselves. It is the features other than these two that are of interest to us. In Fig. 5(a), the suppression of the peak at around an ELF value of 0.5 with increasing pressures is evident, which demonstrates the shift from highly metallic NFE behavior to gradual electron localization. This is accompanied by the formation of a tail in the ELF histogram with values between 0.75 and 0.90. Along the  $T = 300$  K isotherm, this tail feature becomes very prominent in the *hP4* phase, which is characterized by a sharp peak near ELF  $\approx 1$ . Using *a priori* knowledge from the band gap, one would expect this sharp peak to almost completely disappear upon melting-induced metallization. However, this is not seen to be the case and even though the liquid phase is metallic, electron bubbles with paired localization exist in tandem with a NFE distribution. While such localized electronic behavior in the solid state manifests itself in the form of development of the band gap, the liquid phase is metallic. This implies that either these electron bubbles are coalescent in the bands

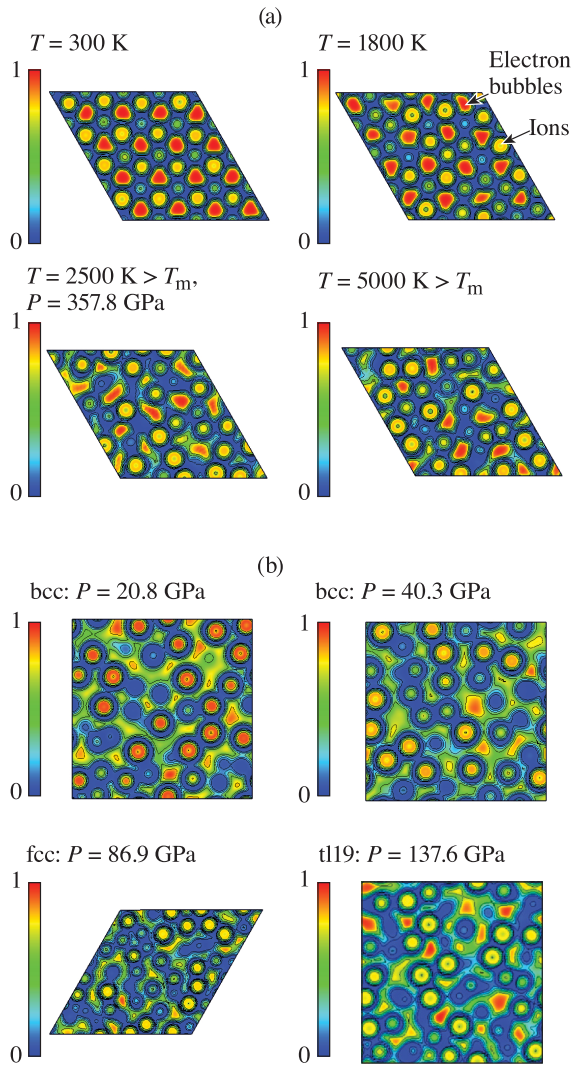


FIG. 4. (a) Planar static ELF on the (001) plane along the  $\rho = 5.872 \text{ g/cm}^3$  isochore, which shows the existence of paired interstitial electrons (red) even beyond the melt point ( $T_m \approx 2100$  to  $2200 \text{ K}$ ). (b) ELF along the  $T = 2500 \text{ K}$  isotherm shows the development of paired interstitial electrons (red) with pressure but NFE-type electronic distribution is also present. The green/yellow spheres correspond to the ions cut along planes that do not pass through their centers.

close to the Fermi level, or despite the decreasing free-electron behavior of the nonbubble electrons at these pressures (relative to liquid sodium at lower pressures), they effectively contribute to the metallization too. However, such electron bubbles ultimately dissipate with increasing temperatures, as can be seen in Fig. 6, where the sharp spike in the ELF histogram tail becomes similar to the behavior of liquid in the  $\sim 80$  to  $\sim 140 \text{ GPa}$  range along the  $T = 2500 \text{ K}$  isotherm. This leads to the conclusion that even though the liquid metal is metallic throughout the pressure domain up to  $\sim 500 \text{ GPa}$ , there are regions in the liquid phase above the  $hP4$ -liquid portion of the melt curve where there exists electron bubbles with  $\text{ELF} \approx 1$ , originating from the delayed dissipation of the localized paired electrons upon melting. Whether these electron bubbles have an effect on the electro-optical properties or not

is explored in the ensuing discussion. In addition, it also needs to be pointed out that the end result of the molecular-dynamics simulations should not depend on the starting symmetry if the target temperature is beyond the melt temperature, and if the simulations are run for a long enough time such that target parameters ( $P$  and  $T$ ) equilibrate. For the purpose of validating that, we did simulations starting with supercells built using bcc and  $tI19$  unit cells. In all such cases, we always observed the formation of the electron bubbles with  $\text{ELF} \approx 1$ .

For a better understanding of this conundrum, the angular momentum ( $l$ )-decomposed electronic density of states are analyzed. Figures 7(a)–7(e) show the evolution of the  $s$ ,  $p$ , and  $d$  components of the electronic DOS with increasing pressure along the  $T = 2500 \text{ K}$  isotherm. Since all of these plots are normalized with respect to the number of atoms in the respective supercell, they can be quantitatively compared. Also, the radius of the projection sphere for computing the partial DOS was set at 65% of the minimum ion-ion neighbor distance at each density. This value was selected after examining the variation of the  $l$ -decomposed DOS when changing the projection sphere radius from 40 to 75% of the minimum neighbor distance and ensuring that the sum of the individual partial DOS was the total DOS. As is evident, the relative contribution of the  $s$  orbitals below the Fermi level gradually decreases with increasing pressure. However, there is a corresponding increase in the contributions of both of the  $p$ - and  $d$  states, manifested as  $p$ - $d$  hybridization in the solid phase [2,4]. Therefore, compressed sodium, whether in the solid or liquid phase, behaves like a transition metal with  $d$ -like electrons. The solid-phase electronic DOS is shown in Fig. 7(f), which shows the  $d$  orbitals becoming dominant in the solid phase. Such  $d$  orbitals contain the bulk of the localized electron pairs in the solid phase and the electron bubbles in the liquid phase, as we will show later. There is also a noticeable increase in the share of  $p$ -orbital electrons in the liquid-phase, as seen in Fig. 7(e), which is a result of the delocalization of the  $p$  electrons in the ELF attractors. The liquid-phase DOS in Fig. 7(e) shows the development of a pseudogap, which implies that bonding exists in the liquid phase. A pseudogap indicates hybridization between the electronic orbitals and, therefore, corresponds to a splitting between bonding and antibonding orbitals on either side of the dip. This is in contrast to lower-pressure liquids which exhibit NFE behavior with no bonding. Using *post hoc* rationalization to determine the hybridization in the liquid phase by comparing the slopes of the  $l$ -decomposed DOS, we conclude that there is  $s$ - $p$  hybridization in liquid sodium.

As a further proof of metallization, Fig. 8 shows the evolution of ac conductivity and reflectivity along (a), (c) the  $\rho = 5.872 \text{ g/cm}^3$  isochore and (b),(d) the  $T = 2500 \text{ K}$  isotherm. All electro-optical calculations were performed with a Gaussian width of  $0.1 \text{ eV}$  (convergence tests shown in sec. IV of the Supplemental Material [26]) and anisotropy was not considered. While moving along the isochore, there is a marked change in the behavior of both reflectivity and ac conductivity once melting takes place. The solid phase plots in Figs. 8(a) and 8(c) have two prominent peaks, in which the first one at  $\sim 5 \text{ eV}$  corresponds to the peak-peak interband transition in the electronic density of states, as can be seen in Fig. 2(b). This peak is characteristic for all insulators and

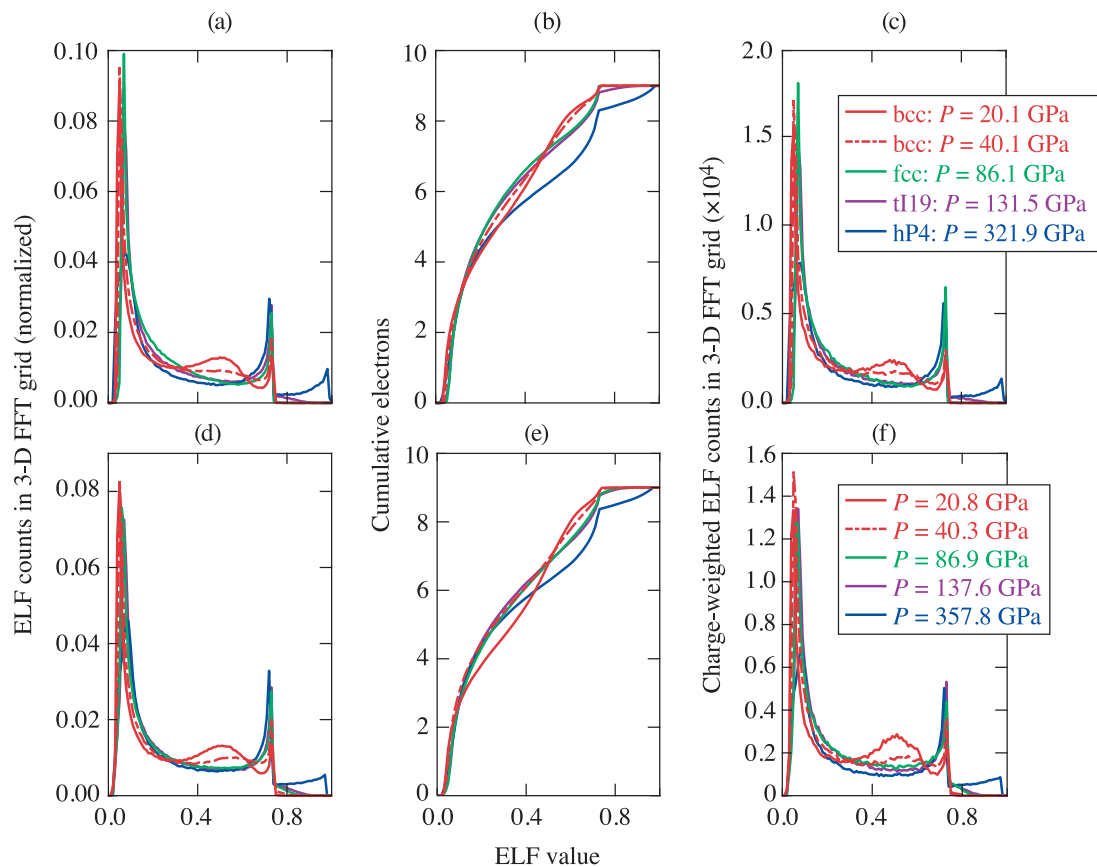


FIG. 5. (a) All-volume ELF histogram, cumulative number of electrons, and charge-weighted all-volume ELF histogram along the  $T = 300$  K isotherm shows the existence of a peak near  $ELF \approx 1$ , corresponding to paired and localized interstitial electrons in the  $hP4$  phase. The peak near  $ELF \approx 0.75$  corresponds to the core electrons. (b) The same plots along the  $T = 2500$  K isotherm, i.e., in the liquid phase, show a similar trend, although the absolute charge value near the  $ELF \approx 1$  peak is lower than the corresponding isochoic solid-state point.

semiconductors with bound charges responding to an impulse from an external electric field. However, all liquid-phase plots in Figs. 8(a)–8(d) exhibit progressively more Drude-like behavior with increasing pressure, as is expected from NFE metallic liquids. While observing the changes along the  $T =$

2500 K isotherm in Figs. 8(b) and 8(d), it can be seen that the dc conductivity (corresponding to  $E = 0$  eV) decreases with increasing pressure along an isotherm. Therefore, from an electro-optical point of view, there is no evidence for a first-order liquid-liquid transition arising out of abrupt

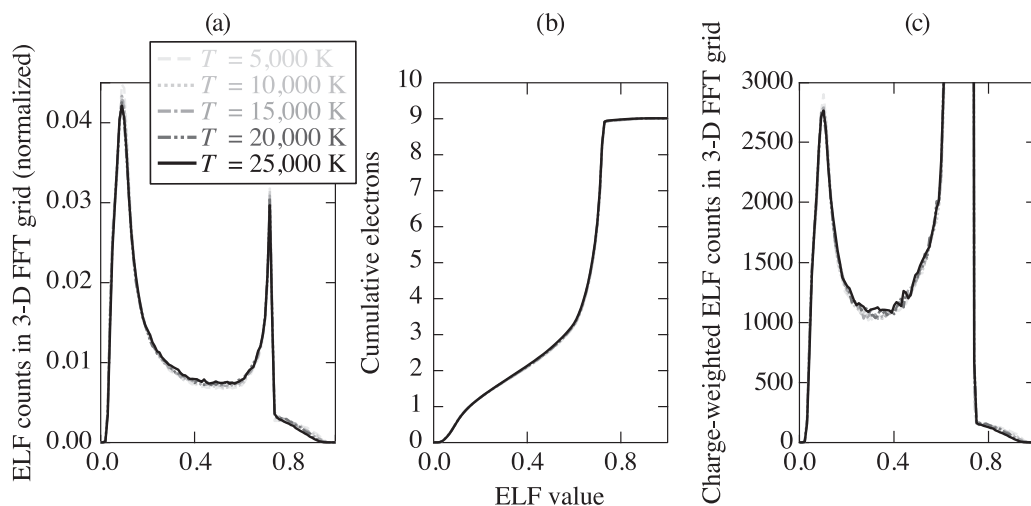


FIG. 6. All-volume ELF histogram, cumulative number of electrons, and charge-weighted ELF histogram along the  $\rho = 5.872$  g/cm<sup>3</sup> isochoic at temperatures far higher than the melt point, demonstrating the dissipation of the localized electron pairs.

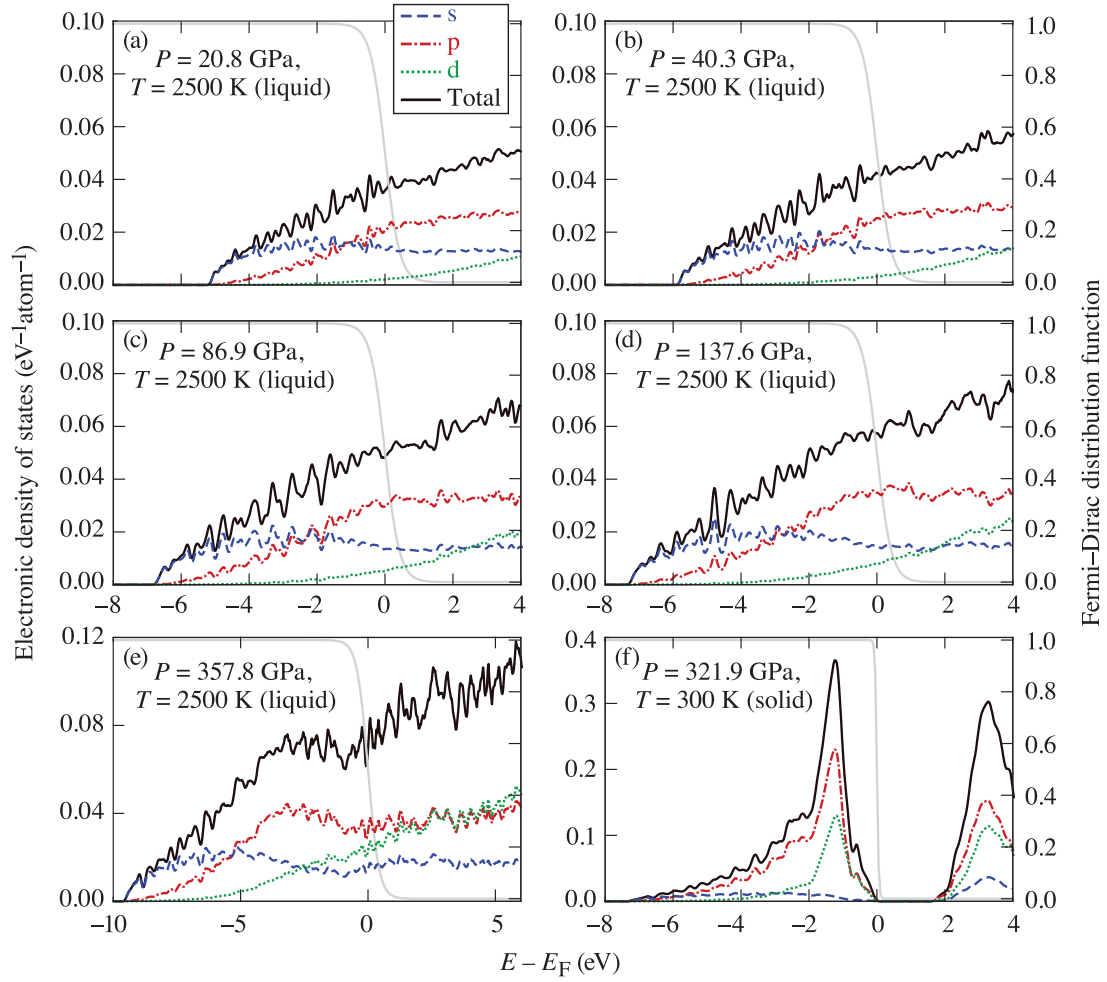


FIG. 7. Evolution of calculated  $l$ -decomposed electronic density of states along the (a)–(e)  $T = 2500$  K isotherm, compared to the (f)  $hP4$  case at  $T = 300$  K. The gray line is the Fermi-Dirac distribution function at the corresponding temperature.

changes in reflectivity and ac conductivity, at least along the liquid isotherm under consideration.

In order to understand the relative contributions of electrons in different orbitals to the dc conductivity, we rewrite the Kubo-Greenwood formula (see Sec. I of the Supplemental Material [26]) in its continuous form as

$$\sigma_1(\omega) \sim \int |\nabla(\varepsilon_i, \varepsilon_j)|^2 \frac{f_{\text{FD}}(\varepsilon_i) - f_{\text{FD}}(\varepsilon_j)}{\varepsilon_j - \varepsilon_i} g(\varepsilon_i) g(\varepsilon_j) d\varepsilon, \quad (9)$$

where  $g(\varepsilon)$  is used to represent the electronic density of states. From the equation above, we argue that the full width at half maximum (FWHM) of the  $(-\partial f_{\text{FD}}/\partial \varepsilon)$  curve can be used as a metric to estimate the range of  $\pm(\varepsilon - E_F)$  values that dominantly determines contribution to dc conductivity, which in the case of the  $\rho = 5.872$  g/cm<sup>3</sup> and  $T = 2500$  K point

corresponds to  $\omega_{\text{FWHM}}$ . The effective number of electrons  $n_{\text{eff}}$  that contribute to the dc conductivity has been estimated using

$$n_{\text{eff}} = \frac{2m_e}{\pi e^2 N} \int_0^{\omega_{\text{FWHM}}} \sigma(\omega) d\omega \quad (10)$$

to be 0.4585, out of which  $s$ ,  $p$ , and  $d$  electrons in the  $0 \leq \omega < \omega_{\text{FWHM}}$  region amount to 0.1569, 0.2232, and 0.0785, respectively. The comparison clearly implies that the  $s$ - $p$  hybridized orbitals contribute predominantly ( $\sim 83\%$ ) to the dc conductivity.

In order to better understand this differentiation between  $s$ - $p$  and  $d$  electrons, we resort to an analytic model. Here, we consider one electron moving through a distribution of ions, that populate the system with density  $\rho \rightarrow \infty$ , as a source of electronic localization. First, we use the Green function for the Schrödinger equation in the Feynman path integral representation [40]:

$$\langle G(\vec{r}(0), \vec{r}(t); t) \rangle = \iiint_{\Omega} \int_{\vec{r}(0)}^{\vec{r}(t)} \exp \left[ -\frac{i}{\hbar} \int_{\tau=0}^t \left\{ \frac{1}{2} m^* \dot{\vec{r}}(\tau)^2 + \sum_j U(\vec{r}(\tau) - \vec{R}_j) \right\} d\tau \right] \delta \vec{r}(\tau) \prod_j \left( \frac{d\vec{R}_j}{\Omega} \right), \quad (11)$$

where  $m^*$  is the effective mass of the electron;  $r$  and  $R_j$  represent the coordinate of the electron and ions, respectively; and  $\Omega$  represents the volume of the system. In the limit  $\Omega \rightarrow \infty$ , with density being finite, the integral over ionic positions can be



computed. This leads to

$$\langle G(\vec{r}(0), \vec{r}(t); t) \rangle = \int_{\vec{r}(0)}^{\vec{r}(t)} \exp \left[ -\frac{i}{\hbar} \int_{\tau=0}^t \frac{1}{2} m^* \dot{\vec{r}}(\tau)^2 d\tau + \rho \iiint_{\Omega} d^3 \vec{R} \left\{ \exp \left[ -\frac{i}{\hbar} \int_{\tau=0}^t U(\vec{r}(\tau) - \vec{R}) \right] - 1 \right\} \right] \delta \vec{r}(\tau). \quad (12)$$

The electronic density of states  $g(E)$  can thereby be obtained using  $r = r'$  and performing a Fourier transform:

$$g(E) = \int_{-\infty}^{\infty} e^{iEt} \langle G(0, t) \rangle dt. \quad (13)$$

Here,  $\langle G(0, t) \rangle$  is analytically continued for negative time and the integral can be evaluated using a Laplace transform with  $t \rightarrow i\tilde{t}$  as

$$g(E) = \int_{c-i\infty}^{c+i\infty} e^{-E\tilde{t}} \zeta(\tilde{t}) d\tilde{t}, \quad (14)$$

where

$$\zeta(\tilde{t}) = \int_{\vec{r}(0)}^{\vec{r}(\tilde{t})} \exp \left[ -\frac{1}{\hbar} \int_{\tau=0}^{\tilde{t}} \frac{1}{2} m^* \dot{\vec{r}}(\tau)^2 d\tau + \rho \iiint_{\Omega} d^3 \vec{R} \left\{ \exp \left[ -\frac{1}{\hbar} \int_0^{\tilde{t}} U(\vec{r}(\tau) - \vec{R}) \right] - 1 \right\} \right] \delta \vec{r}(\tau). \quad (15)$$

Now, in the limit  $\rho \rightarrow \infty$ ,  $\vec{r}(\tilde{t})$  can be approximated as being extremely close to  $\vec{r}(0)$ , which implies electronic localization. Then, the integrand of the second term in the above expression can be rewritten as  $\exp[\rho \iiint_{\Omega} d^3 \vec{R} \exp\{-\frac{iU(\vec{R})}{\hbar}\}]$ .

The above equation, thus, can be expanded in  $\vec{r}(\tau)$  as

$$\begin{aligned} \zeta(\tilde{t}) = \int_{\vec{r}(0)}^{\vec{r}(\tilde{t})} \exp \left[ -\frac{m^*}{2\hbar} \int_{\tau=0}^{\tilde{t}} \dot{\vec{r}}(\tau)^2 - \frac{\rho \bar{U} \tilde{t}}{\hbar} + \frac{\rho \bar{U}^2 \tilde{t}^2}{\hbar^2} \right. \\ \left. - \frac{\rho}{\hbar^2} \bar{U}_g^2 \int_{\tau=0}^{\tilde{t}} \int_{\tau'=0}^{\tilde{t}} \frac{1}{3} \{r(\tau) - r(\tau')\}^2 d\tau d\tau' \right] \delta \vec{r}(\tau), \end{aligned} \quad (16)$$

where  $\bar{U} = \int U d^3 \vec{r}$ ,  $\bar{U}^2 = \int U^2 d^3 \vec{r}$ , and  $\bar{U}_g^2 = \int (\nabla U)^2 d^3 \vec{r}$ . This integral was evaluated with MATHEMATICA yielding the following result:

$$\begin{aligned} g(E) = \int_{c-i\infty}^{c+i\infty} \exp \left\{ -\left( E - \frac{\rho \bar{U}}{\hbar} \right) \tilde{t} + \frac{\rho \bar{U}^2 \tilde{t}^2}{\hbar^2} \right\} \\ \times \left[ \sinh \left\{ \left( \frac{2\rho \bar{U}_g^2}{3\hbar m^*} \right)^{1/2} \tilde{t}^{\frac{3}{2}} \right\} \left( \frac{3\hbar m^*}{2\rho \bar{U}_g^2} \right)^{1/2} \left( \frac{2\pi \hbar}{m^*} \right) \right]^{-3/2} d\tilde{t}. \end{aligned} \quad (17)$$

Figure 9 depicts the electronic DOS of a free-electron gas for two cases with effective mass of the conduction electron, being the actual mass of the electron  $m_e$  and twice  $m_e$ , using a model potential  $U(\mathbf{r}) \propto \exp(-g(\mathbf{r})/k_B T)$ , constructed from the radial distribution function  $g(\mathbf{r})$  calculated from QMD at  $T = 2500$  K. It can be seen that in the case of localization a depression occurs in the electronic DOS deviating from the free-electron parabola. This depression has been referred to as the plasmon onset for conduction electrons [41]. More intense localization, corresponding to higher effective mass, increases the density of states along with delaying the plasmon onset and reduces the chance of hybridization. This will lead to lower contribution of the said electrons to electro-optical properties.

Whereas in the solid state, interstitial electrons are predominantly  $p$ - $d$  hybridized, two separate phenomena take place upon melting: (a) the thermal disorder in the ionic

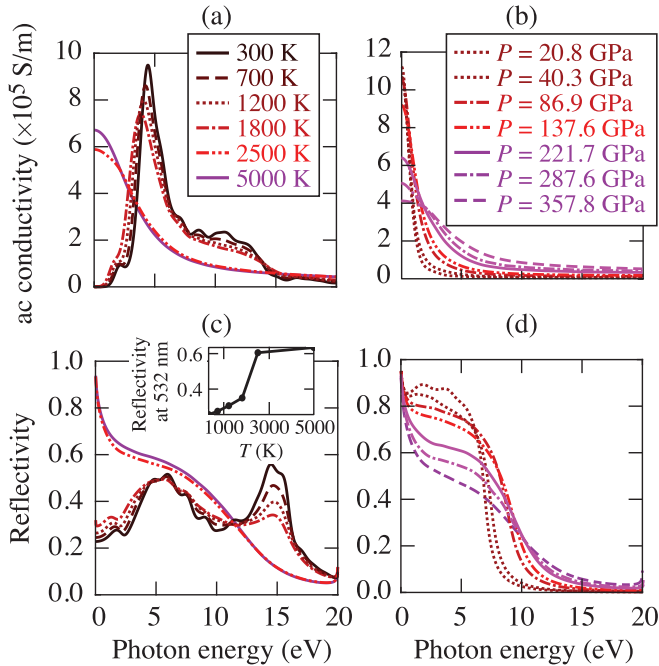


FIG. 8. All-direction averaged electro-optical properties along the (a), (b)  $\rho = 5.872$  g/cm<sup>3</sup> isochores and the (c), (d)  $T = 2500$  K isotherm demonstrating Drude-like behavior with respect to both reflectivity and ac conductivity in the liquid phase. The insulator-to-metal transition is evident from (a) and (c), which demonstrates a distinct qualitative change upon melting at  $T_m \approx 2100$  K that manifests in the form of an abrupt jump in reflectivity along  $\nu = 532$  nm (see inset).

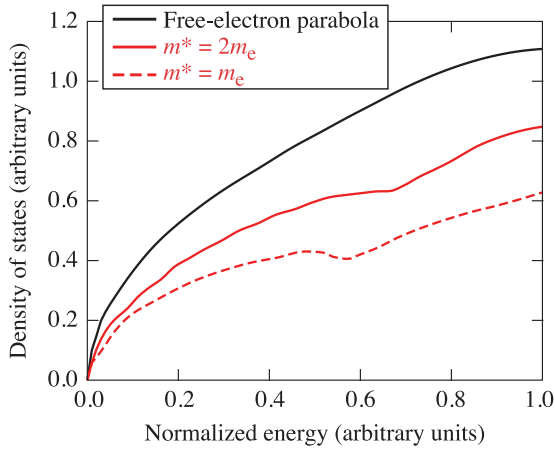


FIG. 9. Electronic density of states derived from our analytic model using a potential obtained from *NVT*-QMD simulations demonstrating the delay of the plasmon onset [39] with increasing effective electron mass. The solid black line corresponds to the free-electron parabola  $g(E) = \frac{1}{2\pi^2} \left(\frac{2m}{\hbar^2}\right)^{3/2} \sqrt{E}$  for spherical surfaces of constant energy with radius in the  $k$  space of  $\frac{\sqrt{2mE}}{\hbar}$ .

configuration in liquids, *vis-à-vis* solids, leads to delocalization [42] of the  $p$  electrons from the  $p$ - $d$  hybridized ELF attractors, alongside drastically increasing the  $s$  character; (b) delayed plasmon onset for  $d$  electrons, beyond 6 eV, as can be seen in Fig. 7(e) compared to  $s$  and  $p$  electrons, due to higher effective mass caused by more localization. The combination of these two effects reduces the contribution of the localized  $d$  electrons in the liquid-phase electron bubbles, despite being coalescent, to conductivity and prevents such electrons from hybridizing.

#### IV. CONCLUSIONS

We have shown that sodium electride in the *hP4* phase can be classified as an insulator using the *nearsightedness* of the one-particle density matrix as a quantitative criterion. In such an insulator system, increasing temperatures along an isochore progressively decreases the electronic band gap. This decrease is primarily driven by the effect of ion dynamics in the solid phase due to its unusual geometry. Upon melting, however, there is a rapid insulator-to-metal transition. This

transition is accompanied by residual electronic localization ( $d$  orbitals) in the form of electron bubbles and a change in electronic orbital hybridization from  $p$ - $d$  to  $s$ - $p$ . The residual electron bubbles are transient in thermodynamic space, and increased temperatures dissipate the said bubbles when the system thermalizes at temperatures away from near-melt conditions. The change in hybridization stems from the fact that increased localization tends to delay the plasmon onset of  $d$  electrons, which decreases their likelihood of hybridization and diminishes their role in electro-optical properties. Such electro-optical properties also demonstrate an insulator-to-metal transition upon melting, along with an unconventional secondary peak in the solid state. However, one open question left unanswered in this paper is the existence of a high-temperature solid phase different from the *hP4* phase. This is not the case along the isochore starting from  $P = 320$  GPa at zero Kelvin, but at higher pressures, we speculate the existence of distorted hexagonal structures. Whether such phases would be insulating or metallic is something worth exploring as well in the future.

#### ACKNOWLEDGMENTS

This material is based upon work supported by the Department of Energy National Nuclear Security Administration under Award No. DE-NA0003856, the University of Rochester, and the New York State Energy Research and Development Authority. S.A.B. performed work at LLNL under the auspices of the US Department of Energy under Contract No. DE-AC52-07NA27344.

This report was prepared as an account of work sponsored by an agency of the U.S. Government. Neither the U.S. Government nor any agency thereof, nor any of their employees, makes any warranty, express or implied, or assumes any legal liability or responsibility for the accuracy, completeness, or usefulness of any information, apparatus, product, or process disclosed, or represents that its use would not infringe privately owned rights. Reference herein to any specific commercial product, process, or service by trade name, trademark, manufacturer, or otherwise does not necessarily constitute or imply its endorsement, recommendation, or favoring by the U.S. Government or any agency thereof. The views and opinions of authors expressed herein do not necessarily state or reflect those of the U.S. Government or any agency thereof.

[1] J. B. Neaton and N. W. Ashcroft, On the Constitution of Sodium at Higher Densities, *Phys. Rev. Lett.* **86**, 2830 (2001).  
 [2] Y. Ma, M. Eremets, A. R. Oganov, Y. Xie, I. Trojan, S. Medvedev, A. O. Lyakhov, M. Valle, and V. Prakapenka, Transparent dense sodium, *Nature (London)* **458**, 182 (2009).  
 [3] M. Marqués, M. Santoro, C. L. Guillaume, F. A. Gorelli, J. Contreras-García, R. T. Howie, A. F. Goncharov, and E. Gregoryanz, Optical and electronic properties of dense sodium, *Phys. Rev. B* **83**, 184106 (2011).  
 [4] A. Lazicki, A. F. Goncharov, V. V. Struzhkin, R. E. Cohen, Z. Liu, E. Gregoryanz, C. Guillaume, H.-K. Mao, and R. J. Hemley, Anomalous optical and electronic properties of dense sodium, *Proc. Nat. Acad. Sci. USA* **106**, 6525 (2009).

[5] M. Gatti, I. V. Tokatly, and A. Rubio, Sodium: A Charge-Transfer Insulator at High Pressures, *Phys. Rev. Lett.* **104**, 216404 (2010).  
 [6] P. Hohenberg and W. Kohn, Inhomogeneous electron gas, *Phys. Rev.* **136**, B864 (1964).  
 [7] W. Kohn and L. J. Sham, Self-consistent equations including exchange and correlation effects, *Phys. Rev.* **140**, A1133 (1965).  
 [8] G. Kresse and J. Hafner, *Ab initio* molecular dynamics for liquid metals, *Phys. Rev. B* **47**, 558 (1993); *Ab initio* molecular-dynamics simulation of the liquid-metal–amorphous-semiconductor transition in germanium, **49**, 14251 (1994).

- [9] G. Kresse and J. Furthmüller, Efficiency of *ab-initio* total energy calculations for metals and semiconductors using a plane-wave basis set, *Comput. Mater. Sci.* **6**, 15 (1996).
- [10] G. Kresse and J. Furthmüller, Efficient iterative schemes for *Ab Initio* total-energy calculations using a plane-wave basis set, *Phys. Rev. B* **54**, 11169 (1996).
- [11] J. P. Perdew, J. A. Chevary, S. H. Vosko, K. A. Jackson, M. R. Pederson, D. J. Singh, and C. Fiolhais, Atoms, molecules, solids, and surfaces: Applications of the generalized gradient approximation for exchange and correlation, *Phys. Rev. B* **46**, 6671 (1992); **48**, 4978(E) (1993).
- [12] D. Mejia-Rodriguez and S. B. Trickey, Deorbitalized meta-GGA exchange-correlation functionals in solids, *Phys. Rev. B* **98**, 115161 (2018).
- [13] J. Sun, A. Ruzsinszky, and J. P. Perdew, Strongly Constrained and Appropriately Normed Semilocal Density Functional, *Phys. Rev. Lett.* **115**, 036402 (2015).
- [14] J. P. Perdew, K. Burke, and M. Ernzerhof, Generalized Gradient Approximation Made Simple, *Phys. Rev. Lett.* **77**, 3865 (1996).
- [15] J. P. Perdew, A. Ruzsinszky, G. I. Csonka, O. A. Vydrov, G. E. Scuseria, L. A. Constantin, X. Zhou, and K. Burke, Restoring the Density-Gradient Expansion for Exchange in Solids and Surfaces, *Phys. Rev. Lett.* **100**, 136406 (2008); **102**, 039902(E) (2009).
- [16] A. Togo, F. Oba, and I. Tanaka, First-principles calculations of the ferroelastic transition between rutile-type and  $\text{CaCl}_2$ -type  $\text{SiO}_2$  at high pressures, *Phys. Rev. B* **78**, 134106 (2008).
- [17] A. Togo, L. Chaput, I. Tanaka, and G. Hug, First-principles phonon calculations of thermal expansion in  $\text{Ti}_3\text{SiC}_2$ ,  $\text{Ti}_3\text{AlC}_2$ , and  $\text{Ti}_3\text{GeC}_2$ , *Phys. Rev. B* **81**, 174301 (2010).
- [18] S. Baroni, S. de Gironcoli, A. Dal Corso, and P. Giannozzi, Phonons and related crystal properties from density-functional perturbation theory, *Rev. Mod. Phys.* **73**, 515 (2001).
- [19] N. D. Mermin, Thermal properties of the inhomogeneous electron gas, *Phys. Rev.* **137**, A1441 (1965).
- [20] R. Kubo, Statistical-mechanical theory of irreversible processes. I. General theory and simple applications to magnetic and conduction problems, *J. Phys. Soc. Jpn.* **12**, 570 (1957).
- [21] D. A. Greenwood, The Boltzmann equation in the theory of electrical conduction in metals, *Proc. Phys. Soc. Lond.* **71**, 585 (1958).
- [22] A. Baldereschi, Mean-value point in the Brillouin zone, *Phys. Rev. B* **7**, 5212 (1973).
- [23] H. J. Monkhorst and J. D. Pack, Special points for Brillouin-zone integrations, *Phys. Rev. B* **13**, 5188 (1976).
- [24] P. E. Blöchl, Projector augmented-wave method, *Phys. Rev. B* **50**, 17953 (1994).
- [25] G. Kresse and D. Joubert, From ultrasoft pseudopotentials to the projector augmented-wave method, *Phys. Rev. B* **59**, 1758 (1999).
- [26] See Supplemental Material at <http://link.aps.org/supplemental/10.1103/PhysRevB.102.094103> for a more detailed description of the computational method and convergence tests, which includes Refs. [20,21].
- [27] P. B. Allen and M. Cardona, Theory of the temperature dependence of the direct gap of germanium, *Phys. Rev. B* **23**, 1495 (1981).
- [28] P. B. Allen and V. Heine, Theory of the temperature dependence of electronic band structures, *J. Phys. C: Solid State Phys.* **9**, 2305 (1976).
- [29] S. Nosé, A molecular dynamics method for simulations in the canonical ensemble, *Mol. Phys.* **52**, 255 (1984).
- [30] E. Gregoryanz, O. Degtyareva, M. Somayazulu, R. J. Hemley, and H.-K. Mao, Melting of Dense Sodium, *Phys. Rev. Lett.* **94**, 185502 (2005).
- [31] R. Paul, S. X. Hu, and V. V. Karasiev, Anharmonic and Anomalous Trends in the High-Pressure Phase Diagram of Silicon, *Phys. Rev. Lett.* **122**, 125701 (2019).
- [32] R. Paul, S. X. Hu, and V. V. Karasiev, Crystalline phase transitions and vibrational spectra of silicon up to multiterapascal pressures, *Phys. Rev. B* **100**, 144101 (2019).
- [33] V. V. Kechin, Thermodynamically based melting-curve equation, *J. Phys.: Condens. Matter* **7**, 531 (1995).
- [34] Y. Li, Y. Wang, C. J. Pickard, R. J. Needs, Y. Wang, and Y. Ma, Metallic Icosahedron Phase of Sodium at Terapascal Pressures, *Phys. Rev. Lett.* **114**, 125501 (2015).
- [35] S. Ismail-Beigi and T. A. Arias, Locality of the Density Matrix in Metals, Semiconductors, and Insulators, *Phys. Rev. Lett.* **82**, 2127 (1999).
- [36] W. Kohn, Density Functional and Density Matrix Method Scaling Linearly with the Number of Atoms, *Phys. Rev. Lett.* **76**, 3168 (1996).
- [37] S. Poncé, E. R. Margine, C. Verdi, and F. Giustino, EPW: Electron-phonon coupling, transport and superconducting properties using maximally localized Wannier functions, *Comput. Phys. Commun.* **209**, 116 (2016).
- [38] A. D. Becke and K. E. Edgecombe, A simple measure of electron localization in atomic and molecular systems, *J. Chem. Phys.* **92**, 5397 (1990).
- [39] I. Tamblyn, J.-Y. Raty, and S. A. Boney, Tetrahedral Clustering in Molten Lithium under Pressure, *Phys. Rev. Lett.* **101**, 075703 (2008).
- [40] I. M. Gel'fand and A. M. Yaglom, Integration in functional spaces and its applications in quantum physics, *J. Math. Phys.* **1**, 48 (1960).
- [41] L. Hedin, B. I. Lundqvist, and S. Lundqvist, Beyond the one-electron approximation: Density of states for interacting electrons, in *Electronic Density of States*, edited by L. H. Bennett, NBS Special Publication 323 (National Bureau of Standards, Washington, D.C., 1968), p. 233.
- [42] J.-Y. Raty, E. Schwegler, and S. A. Boney, Electronic and structural transitions in dense liquid sodium, *Nature (London)* **449**, 448 (2007).